Green Chemistry

PAPER

View Article Online
View Journal | View Issue

Cite this: *Green Chem.*, 2025, **27**, 11517

Electrochemical upgrading of 5-hydroxymethylfurfural *via* a defect-rich $NiCo_2O_4$ array

Xiao Zhou,†[a] Zhixian Mao,†[b] Wen Li,†[a] Zeting Gong,[c] Wanxin Liu,[a] Yi Li,[a] Di Yin,[a] Yijin Wu, *[a,b] Yongsheng Yao*[c] and Xiaolin Wei *[c]

Received 16th June 2025,
Accepted 26th August 2025

DOI: 10.1039/d5gc03049h

rsc.li/greenchem

Regulation of the surface evolution and kinetic behavior of interfacial molecules by defect engineering is significant for the efficient production of the value-added chemical 2,5-furandicarboxylic (FDCA) through the electrochemical oxidation of 5-hydroxymethylfurfural (HMFOR). Herein, a precatalyst array ($NiCo_2O_4$-mV) assembled from $NiCo_2O_4$ nanoparticles (~10 nm) with mixed-ionic defect species (m-Ds) was synthesized. *In situ* Raman spectroscopy shows that as the potential increases, the partial surface of $NiCo_2O_4$-mV formed an $NiCo_2O_4$/NiCoO(OH) heterojunction on the catalyst surface. *Operando* ATR-SEIRAS and DE-MS measurements further reveal that the built-in electric field derived from this heterojunction leads to a decrease in the coverage of adsorbed water molecules at the electrode–electrolyte interface, thereby promoting the adsorption and efficient mass transfer of HMF molecules, ultimately obtaining an industrial-level current density (1 A@1.636 V). This work further elucidates the structure–activity relationship for defect-rich precatalysts in the electrooxidation of organic compounds.

Green foundation

1. This work presents the successful preparation of a $NiCo_2O_4$ array catalyst ($NiCo_2O_4$-mV) with mixed-ionic defects, which exhibits excellent HMFOR performance with industrial-level current density (1.329 A cm^{-2}@1.7 V), an outstanding FDCA yield (99.6%), high faradaic efficiency (95.7%) and robust cycling stability.
2. A series of *in situ* characterization studies have demonstrated that defect-rich-induced partial surface reconstruction forms a $NiCo_2O_4$/NiCoO(OH) heterojunction interface, which facilitates the kinetic adsorption of HMF molecules at the interface while, in contrast, inhibiting water.
3. In the future, we will focus on constructing high-performance decoupled catalysts to address (1) efficient HMFOR performance under non-alkaline conditions and (2) environmentally friendly and membrane-free HMFOR systems.

1. Introduction

To address the severe challenges relating to energy security, environmental pollution and climate change, the establishment of sustainable systems for synthesizing bulk fuels and chemicals from renewable biomass resources has been considered an important strategic approach as part of the current global energy transition.[1] In recent years, 5-hydroxymethylfurfural (HMF), as a renewable biomass platform molecule, has gained attention due to its key oxidized product, 2,5-furandicarboxylic acid (FDCA), which is an important fine chemical and can be used as a monomer in the industrial production of polyamides, polyesters, and polyurethanes, as well as being a replacement for phthalic acid.[2] Therefore, the electrochemical oxidation of HMF (HMFOR), which can be coupled with water electrolysis for hydrogen production at normal temperature and pressure with high selectivity, can not only produce the high-value-added chemical FDCA, but also reduce the cell voltage of water electrolysis for hydrogen production, achieving two goals with one action.[3] This has provided a solid opportunity for promoting the global implementation of a grand strategy for the high-quality development of renewable energy.

Currently, the large-scale commercialization of FDCA preparation through HMFOR faces numerous challenges. The construction of high-performance and low-cost electrocatalysts is a significant factor in overcoming these challenges. Various non-noble metal electrocatalysts, including metallic oxygen

[a]*Hunan Engineering Research Center for monitoring and treatment of heavy metals pollution in the upper reaches of XiangJiang River, Key Laboratory of Functional Metal–Organic Compounds of Hunan Province, College of Chemistry and Material Science, Hengyang Normal University, Hengyang 421002, P. R. China. E-mail: yjwu@issp.ac.cn, wuyj313978@163.com*
[b]*Centre for Environmental and Energy Nanomaterials, Institute of Solid State Physics, Hefei Institutes of Physical Science, Chinese Academy of Sciences, Hefei, Anhui 230031, China*
[c]*College of Physics and Electronics Engineering, Hengyang Normal University, Hengyang 421002, P. R. China. E-mail: yaoys@hynu.edu.cn, xlw@xtu.edu.cn*
†These authors contributed equally.

compounds (oxides,[4,5] hydroxides,[6,7] and oxyhydroxides[8–10]), sulfides,[11,12] phosphides,[13,14] carbides,[15,16] boride,[17] metal complexes,[18,19] *etc*., have been developed, and their structure–activity relationships have been studied. Particularly, Ni-based electrocatalysts, with their abundant 3d electrons and easily tunable e_g orbitals, can effectively manage the covalency of metal–oxygen bonding, thereby optimizing the adsorption/desorption behaviors of intermediates such as HMF and significantly improving the performance of HMFOR.[6] Emphatically, when the applied potential exceeds 1.4 V, Ni-based oxyhydroxides with higher HMFOR activity often evolve from Ni-based hydroxides through the electrochemical dehydrogenation of lattice hydroxyl groups induced by high reaction potentials.[5,9,20] However, for another type of high-HMFOR-activity Ni-based transition-metal spinel oxides,[21–23] which also belong to the category of Ni-based oxides, efficiently converting them into Ni-based hydroxides at low potentials is a nonnegligible prerequisite for the formation of highly active Ni-based oxyhydroxide species.

For the efficient evolution of Ni-based transition-metal spinel oxides to Ni-based hydroxides and even oxyhydroxides, the local coordination/electronic structure of the surface of transition-metal spinel oxides (most spinel oxides often possess cationic defects due to excess non-stoichiometric oxygen) can be regulated by a defect engineering strategy, thereby enhancing the electrocatalytic activity of the catalysts.[24] It has been reported that under the drive of an applied potential, cationic defects can activate adjacent metal active components to undergo surface evolution and then form highly active oxyhydroxide species due to the inherent relative instability of the defect sites.[25–27] However, in fact, during the structural evolution, a heterogeneous interface between oxides and hydroxides/oxyhydroxides will be generated.[28] Furthermore, due to the potential difference caused by the interfacial polarization resulting from the bandgap differences of the two heterogeneous phases, an internal built-in electric field (BIEF) will eventually be formed.[29] The BIEF further modulates the electronic structure of the active sites, optimizing the reaction microenvironment on the surface of the electrocatalyst and the adsorption/desorption energy barriers of the key intermediates.[29–31] Nevertheless, in the field of HMFOR, the charge redistribution process between the local defect sites and active sites and the interaction mechanism between the heterogeneous interface and the reaction species (such as HMF, HMF intermediates, interfacial water, *etc*.) remain elusive and require further investigation by scientists.

Herein, as shown in Fig. 1a, we report that a $NiCo_2O_4$ array ($NiCo_2O_4$-mV) containing m-Ds was obtained through a simple hydrothermal method in alkaline solution. Moreover, an integrated evaluation of the dynamic structural evolution of the catalyst and HMF molecules during the HMFOR process was carried out using a comprehensive testing system combining *in situ* Raman, ATR-SEIRAS and DEMS studies with *ex situ* XAFS. The results indicate that the existence of the aforementioned m-Ds leads to the elongation of M–M bonds and Ni–O bonds and the enhancing of more highly oxidative $M^{(2+\delta)+}$ ($0 < \delta < 0$) species in the catalyst. Meanwhile, due to the presence of m-Ds and high-valence $M^{(2+\delta)+}$ species in the catalyst, dynamic structural evolution occurs at a low potential, and an evolution path from $NiCo_2O_4$-mV → $Ni(OH)_2$ → NiOOH is formed as the applied potential continuously increases. Particularly, the NiOOH species that evolved at high potentials form a heterojunction with bulk $NiCo_2O_4$. This results in the rearrangement of electrons at the heterogeneous interface and the generation of interfacial potential oscillations, which suppress the adsorption of interfacial water molecules and enhance the rapid mass transfer of HMF molecules due to the formation of an inhomogeneous BIEF at the heterojunction interface, thereby improving the activity and selectivity of HMFOR. As expected, $NiCo_2O_4$-mV exhibits excellent HMFOR performance with industrial-level current density, an outstanding FDCA yield, high faradaic efficiency and robust cycling stability.

2. Experimental section

2.1. Chemicals and materials

Nickel foam (thickness of 1 mm) was purchased from Suzhou Shengernuo Technology (Chain) Co., Ltd. Cobalt(II) nitrate hexahydrate ($Co(NO_3)_2{\cdot}6H_2O$, ≥99%), nickel(II) nitrate hexahydrate ($Ni(NO_3)_2{\cdot}6H_2O$, ≥99%), urea ($CO(NH_2)_2$, ≥99%), ammonium fluoride (NH_4F, ≥98%), ethanol (AR, ≥99.5%), acetone (AR, ≥99.5%), 5-hydroxymethyl-2-furaldehyde (AR, ≥99.5%), 5-hydroxymethyl-2-furoic acid (HMFCA, ≥98%), 2,5-furandicarboxaldehyde (DFF, ≥98%), 5-formyl-2-furoic acid (FFCA, ≥96%), and 2,5-furandicarboxylic acid (FDCA, ≥98%) were purchased from Sinopharm Chemical Reagent Co., Ltd. Potassium hydroxide (KOH, 95%) was purchased from Meryer (Shanghai) Chemical Technology Co., Ltd. Nafion (5%) was purchased from Sigma-Aldrich.

2.2. Preparation of electrocatalysts

Nickel(II) nitrate hexahydrate (2.2 mM), ammonium fluoride (4.2 mM), urea (10 mM), cobalt(II) nitrate hexahydrate (8 mM), and 40 mL of distilled water were sequentially introduced into a hydrothermal reaction vessel lined with an inner lining. The mixture was subjected to ultrasonication for 30 minutes to ensure the homogeneous distribution of the reactants. Following this, one piece of cleaned nickel foam (1.5 × 0.5 cm) was immersed in the aforementioned solution, which was then sealed within a stainless-steel reaction vessel and maintained at 120 °C for 2 hours. The product obtained was subsequently washed three times with distilled water and ethanol and then placed in a drying oven at 60 °C for drying. The as-obtained product, after drying, was subjected to calcination in a muffle furnace at a temperature of 300 °C for 6 hours at a heating rate of 5 °C min^{-1}, supporting the formation of a $NiCo_2O_4$ array. Finally, the $NiCo_2O_4$ array was again subjected to a similar hydrothermal process, without the addition of metal salts at 120/130/140/150 °C for 3 hours.

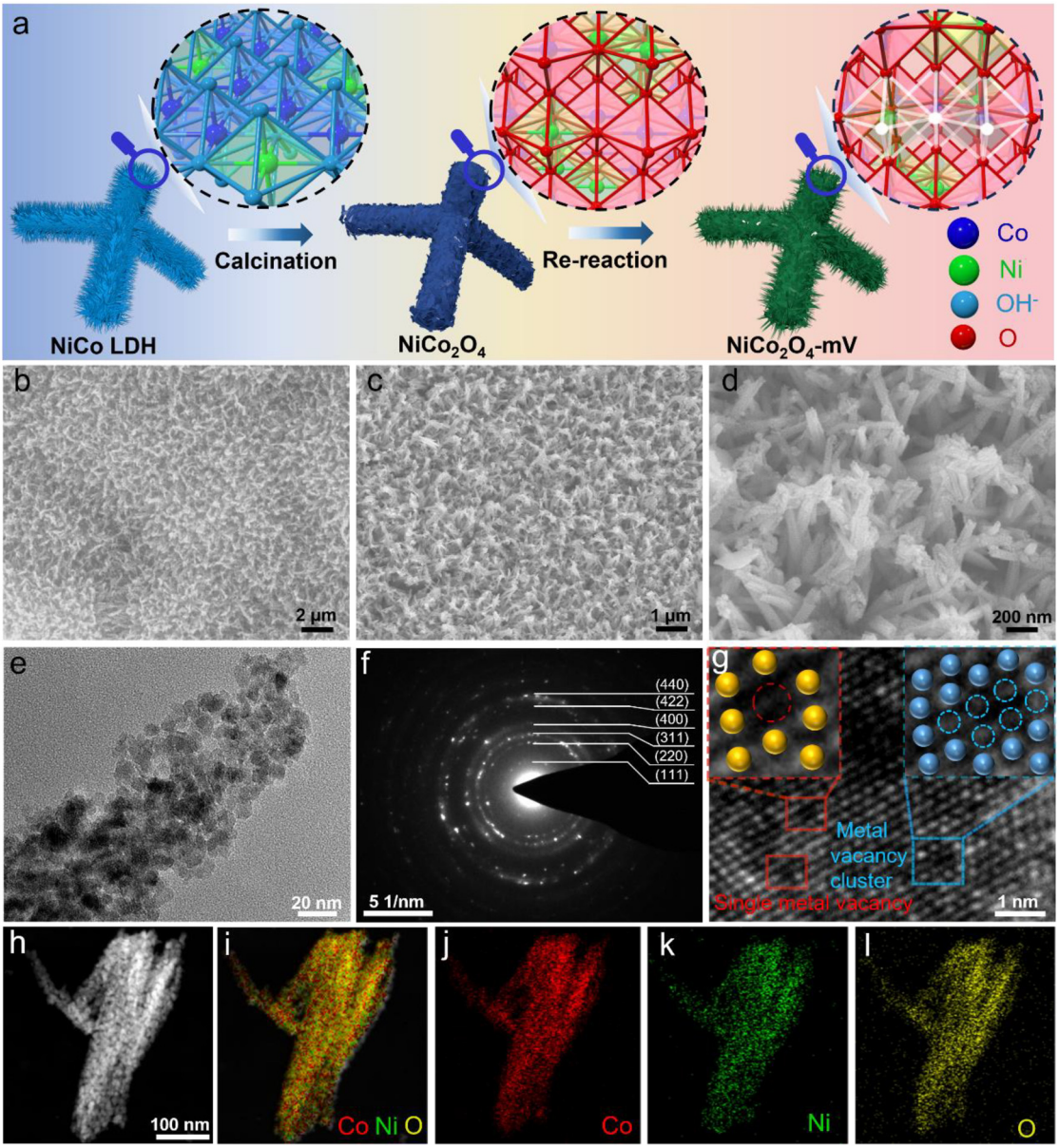

Fig. 1 (a) A schematic illustration of the fabrication and local conversion of crystalline $NiCo_2O_4$-mV; SEM images of (b) $NiCo_2O_4$ and $NiCo_2O_4$-mV at (c) low magnification and (d) high magnification; (e and g) HR-TEM images of $NiCo_2O_4$-mV with different defect structures; (f) the SAED pattern of $NiCo_2O_4$-mV; and (h–l) EDX elemental mapping of $NiCo_2O_4$-mV.

2.3. Material characterization

Powder X-ray diffraction (PXRD) measurements were made using a Philips X-Pert Pro X-ray diffractometer with Cu Kα radiation (λ = 1.5418 Å) at a generator current of 40 mA with a scan range of 10–80°. Scanning electron microscopy (SEM) was performed using a Hitachi (SU8020) microscope operated at 5.0 kV. A ThermoFisher Scientific Talos F200x-type transmission electron microscope (TEM) was used. The distribution of the corresponding elements on the catalyst surface was obtained by energy-dispersive X-ray spectroscopy (EDS) using TEM. The surface element compositions and atomic valence states of the catalysts were determined using an ESCALAB 250Xi X-ray photoelectron spectrometer (XPS). A voltage window of 3.0–4.3 V at 40 mA g^{-1} served as the setting for X-ray absorption spectroscopy (XAS) experiments conducted using TableXAFS-500 apparatus (Anhui Chuangpu Instrument Technology Co., Ltd). Data treatment and data analysis were carried out *via* Athena software. *In situ* Raman spectra were recorded with an Xplora confocal microprobe Raman system (HORIBA JobinYvon). *In situ* attenuated total reflection surface-enhanced infrared absorption spectroscopy (ATR-SEIRAS) data was obtained using a Nicolet Nexus FT-IR spectrometer. Operando differential electrochemical mass spectroscopy analysis with isotope

labeling measurements was carried out in an electrochemical cell with a typical three-electrode system using a QAS 100 device (Linglu Instruments, Shanghai).

2.4. Electrochemical measurements

All electrochemical tests were conducted by using a CS2350M electrochemical workstation (Wuhan Corrtest Instruments Co., Ltd, China) in a three-electrode system. Catalyst with an effective area of 1 × 0.5 cm^2 was used as the working electrode, while a graphite rod and Hg/HgO electrode were used as the counter and reference electrodes, respectively. All data were reported with 95% ohmic drop compensation. All potentials given in this research were referenced to a reversible hydrogen electrode (RHE) according to the following equation: $E_{RHE} = E_{Hg/HgO} + 0.098 + 0.0591 \times pH - 95\%iR$, where i is the measured current and R is the uncompensated resistance determined by impedance analysis. Oxygen evolution reaction (OER) performances were tested in 1.0 M KOH electrolyte in an H-shaped cell, and HMFOR tests involved the addition of 50 mM HMF to the 1.0 KOH solution. Linear scanning voltammetry curves (LSV) were obtained at a scan rate of 5 mV s^{-1}. Electrochemical impedance spectroscopy (EIS) analysis was carried out in the 0.01–100 000 Hz range at different potentials. The electrochemical surface area (ECSA) was evaluated by using double-layer capacitance (C_{dl}). Cyclic voltammetry (CV) analysis was conducted in 1.0 M KOH + 50 mM HMF in the non-faradaic regions of 1.0–1.1 V at different scan rates of 5, 10, 20, 40, 80, 100 and 120 mV s^{-1}. Chronopotentiometry (CP) tests were conducted in 1.0 M KOH + 50 mM HMF at 50 mA cm^{-2} for 5 h.

2.5. HPLC analysis

HMF electrooxidation was conducted through using a chronoamperometry method at a potential of 1.4 V. Measurements were performed with 20 mL of KOH + 10 mM HMF in the anode chamber and 15 mL of KOH in the cathode chamber in an H-type electrolytic cell. A volume of 50 μL of electrolyte from the anode compartment was diluted with purified water to 2 mL, and the resulting solution was subjected to high-performance liquid chromatography (HPLC, Waters 1525) analysis at room temperature using a UV-visible detector at a detection wavelength of 265 nm. The HPLC system was equipped with a C18 column (4.6 mm × 150 mm, Shim-pack GWS, 5 μm); mobile phase A: methanol, and B: 5 mM ammonium formate aqueous solution; A : B = 3 : 7; flow rate: 0.6 ml min^{-1}.

2.6. Differential electrochemical mass spectroscopy (DEMS) measurements

Operando differential electrochemical mass spectroscopy measurements were carried out in an electrochemical cell with a three-electrode system using the QAS 100 device (Linglu Instruments, Shanghai). $NiCo_2O_4$ or $NiCo_2O_4$-mV, a Hg/HgO electrode and pure Pt wire were used as the WE, RE and CE, respectively. A capillary quartz probe filled with hydrophobic PTFE paper was placed above the working electrode. Subsequently, after assembling the three-electrode system, voltages ranging from 1 to 1.7 V (each voltage was applied for 200 s) were applied to the working electrode, and gaseous products were collected for further analysis.

3. Results and discussion

3.1. Characterization of $NiCo_2O_4$-mV

Inspired by defect engineering, $NiCo_2O_4$-mV with m-Ds was constructed *via* an alkaline solution hydrothermal method. As shown in Fig. 1a, the synthesis of $NiCo_2O_4$-mV involved a NiCo layered double hydroxide grown on the NF substrate undergoing an air calcination-hydrothermal process. The XRD patterns (Fig. S1) exhibited a slightly weaker diffraction intensity of the $NiCo_2O_4$ phase (JCPDS no. 20-0781) compared to the original $NiCo_2O_4$, indicating that the existence of m-Ds in bulk $NiCo_2O_4$-mV reduced the crystallinity of the catalyst. SEM images of $NiCo_2O_4$-mV grown on the NF substrate revealed a morphology of nanorods with a micron-scale length and a width of ~100 nm (Fig. 1c and d and Fig. S1a–c). The surface of $NiCo_2O_4$-mV showed a morphological transformation from smooth to partially wrinkled compared to original $NiCo_2O_4$. TEM images further revealed that the $NiCo_2O_4$-mV nanorods are assembled from numerous nanoparticles with diameters of ~10 nm (Fig. 1e). These small-sized $NiCo_2O_4$-mV nanoparticles could facilitate the exposure of a greater surface area and unsaturated active sites during electrocatalysis processes. Furthermore, the SAED pattern in Fig. 1f clearly identifies the polycrystalline structure belonging to $NiCo_2O_4$. More importantly, HR-TEM images further presented clear evidence of the coexistence of single metal defects and metal defect clusters, confirming the presence m-Ds in $NiCo_2O_4$-mV (Fig. 1g). The uniform distribution of Ni, Co and O elements in $NiCo_2O_4$-mV was displayed by EDS elemental mapping analysis (Fig. 1h–l).

Defect engineering is known to affect the surface environment of catalysts, thereby modulating the local electronic structure of active metals. A significant positive shift in binding energies, seen based on deconvoluted Co and Ni 2p spectra, confirms the high oxidation states of Co and Ni induced by m-Ds in $NiCo_2O_4$-mV. Specifically, compared to $NiCo_2O_4$, the binding energy of the Co $2p_{3/2}$ peak in $NiCo_2O_4$-mV is observed to shift positively by 0.15 eV (Fig. 2a). Additionally, the ratio of the Co^{3+}/Co^{2+} photoelectron peaks in $NiCo_2O_4$-mV increased from 0.39 to 0.61, indicating the presence of extensive cationic defects, leading to the generation of $Co^{(2+\delta)+}$ ($0 < \delta < 1$) in this sample. Similarly, for the Ni $2p_{3/2}$ peak, unlike the single Ni^{2+} photoelectron peak in $NiCo_2O_4$, two spin-split peaks located at 855.2 and 856.9 eV, attributed to Ni^{2+} and Ni^{3+}, were distinctly observed in $NiCo_2O_4$-mV with a high Ni^{2+}/Ni^{3+} ratio of 0.31, supporting the generation of the higher valence state of $Ni^{(2+\delta)+}$ ($0 < \delta < 1$) in $NiCo_2O_4$-mV (Fig. 2b). The O 1s spectrum (Fig. 2c and Fig. S3b and c) could be deconvoluted into peaks corresponding to lattice oxygen, M–O–M, dangling oxygen bonds and adsorbed H_2O. Compared to $NiCo_2O_4$, the first three photoelectron peaks in $NiCo_2O_4$-mV exhibit a negative shift of about 0.2 eV. These

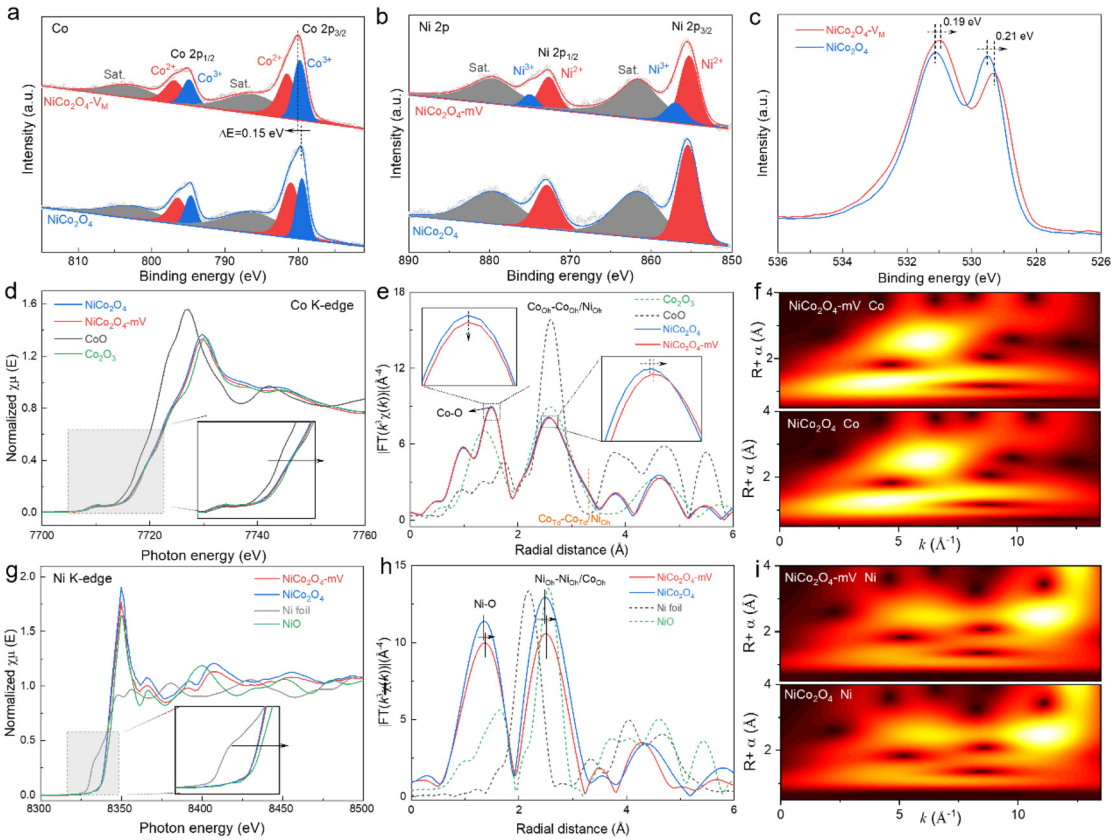

Fig. 2 (a) Co 2p, (b) Ni 2p, and (c) O 1s XPS spectra for $NiCo_2O_4$-mV and $NiCo_2O_4$; XANES spectra of the (d) Co and (g) Ni K-edge with a zoomed-in view of the pre-peak region in the insets; the corresponding k^3-weighted Fourier-transformed EXAFS R-space patterns for (e) Co and (h) Ni in different samples; and WT-EXAFS spectra for (f) Co and (i) Ni from $NiCo_2O_4$-mV and $NiCo_2O_4$.

results illustrate well that the partial electron transfer from Co/Ni metal ions to oxygen atoms through intracrystalline metal–oxygen (M–O) bonds, induced by cationic defects, leads to an increase in the valence states of partial surface metal atoms.[32]

The influence of cationic defects on the local electronic structure of m-Ds is further confirmed by XANES (Fig. 2d and g). Compared with standard samples and pristine $NiCo_2O_4$, the normalized Co and Ni K-edge XANES spectra of $NiCo_2O_4$-mV are observed to shift towards higher energies, indicating an increase in the oxidation states of Co and Ni. This result is consistent with the oxidation state variation behavior observed in the XPS spectra. Further FT-EXAFS is employed to determine the coordination environment and local atomic configuration of the catalyst (Fig. 2e and h). For the Co and Ni K-edge FT-EXAFS spectra of $NiCo_2O_4$-mV, the peaks correspond to Co/Ni–O, Co/Ni–Co/Ni, and Co–Co/Ni, representing the coordination of Co/Ni–O, Co_{Oh}–Co_{Oh}/Ni_{Oh} and Ni_{Oh}–Ni_{Oh}/Co_{Oh}, and Co_{Td}–Co_{Td}/Ni_{Oh} shells, respectively.[33] Specifically, no tetrahedral Ni sites are observed in $NiCo_2O_4$-mV, indicating that all Ni sites occupy octahedral sites. Interestingly, compared with original $NiCo_2O_4$, $NiCo_2O_4$-mV exhibits longer bond lengths for the Ni–O and Co_{Oh}/Ni_{Oh}–Co_{Oh}/Ni_{Oh} shells. Similar results are found in the wavelet transform (WT) analysis of Co and Ni K-edge data for both $NiCo_2O_4$ samples (Fig. 2f and i).

It is well known that the chemical formula of the spinel structure is AB_2O_4, where A and B are two different metal cations. When A^{2+} occupies the tetrahedral (Td, oxygen coordination: 4) site and B^{3+} occupies the octahedral site (Oh, oxygen coordination: 6), a standard spinel structure is formed. From the XANES and EXAFS results of the two $NiCo_2O_4$ catalysts, it can be seen that more high-valent $Co^{(2+\delta)+}$/$Ni^{(2+\delta)+}$ species are generated in $NiCo_2O_4$-mV, where Co^{3+}/Ni^{3+} mainly occupies octahedral Co_{Oh} or Ni_{Oh} sites, while Co^{2+}/Ni^{2+} occupies tetrahedral Ni_{Td} sites. The formation of a strong Jahn–Teller effect caused by the oxidation state of high-valent Co/Ni ions leads to octahedral lattice elongation, inducing an increase in the mean square disorder on the catalyst surface, which might ultimately adjust the surface energy of the catalyst and the adsorption/desorption energy barriers of oxygen-containing intermediates.[34] Similar lattice distortion phenomena have been extensively reported in previous literature.[35–37] Moreover, compared with the Co and Ni K-edge EXAFS spectra of $NiCo_2O_4$, the amplitudes of the Co and Ni characteristic peaks in $NiCo_2O_4$-mV are reduced. Particularly, the Ni element exhibits a significantly greater decrease compared to that of Co (Fig. 2e and h). This may be related to the atomic coordination number and mean square disorder of the catalyst, that is, a low coordination number and large mean square disorder

correspond to a small amplitude.[33] The aforementioned results strongly demonstrate the presence of mixed-ionic defects in $NiCo_2O_4$-mV, as well as a greater abundance of Ni ion defects, attributed to the increased surface disorder induced by cationic defects. The m-Ds on the $NiCo_2O_4$-mV surface, coupled with the strong Jahn–Teller effect, might be crucial for rapid electron transfer and multi-step surface evolution toward $NiCo_2O_4$-mV during the HMFOR process. UV-DRS was used to study the effects of the introduction of m-Ds on the band gaps of the two aforementioned $NiCo_2O_4$ samples. As shown in Fig. S5, the UV-DRS-determined band gap energy (E_g) results reveal a smaller E_g value (1.20 eV) for $NiCo_2O_4$-mV compared with $NiCo_2O_4$ (1.42 eV). The above results indicate that a smaller band gap increases the probability of a valence electron jumping to the conduction band in $NiCo_2O_4$-mV, ultimately increasing the conductivity of $NiCo_2O_4$-mV and thereby enhancing the HMFOR activity. The characterization of the local coordination/electronic structures of this catalyst once again illustrates the significant impact of m-Ds on the bulk and surface structures of $NiCo_2O_4$.

3.2. Electrochemical performance of the catalyst

The HMFOR and OER performances of $NiCo_2O_4$-mV were evaluated using a typical three-electrode system in 1.0 M KOH electrolyte with/without 50 mM HMF. Initially, cyclic voltammetry (CV) was conducted to investigate the electrochemical behavior of the reversible oxidation and reduction of the active species of the catalyst in different electrolytes. As illustrated in Fig. S6a, both $NiCo_2O_4$-mV and $NiCo_2O_4$ exhibit a redox couple (E_p and E'_p) in 1 M KOH solution, with these E_p/E'_p peaks being attributed to the redox couple of M^{2+}/M^{3+} (where M = Ni, Co). Compared to the E_p/E'_p peaks of $NiCo_2O_4$, the E_p/E'_p peaks of $NiCo_2O_4$-mV appear at lower potentials, indicating that the mixed-ionic defects in $NiCo_2O_4$-mV facilitate the formation of higher-valent species at lower potentials in 1 M KOH solution. In contrast, when the electrolyte contains 50 mM HMF, a rapid increase in anodic current density is observed (Fig. S6b and c), demonstrating the excellent catalytic activity of both $NiCo_2O_4$-mV and $NiCo_2O_4$ towards HMFOR. As seen from the LSV curves in Fig. 3a, compared with the reference electrolyte without HMF, the potential required for $NiCo_2O_4$-mV at a current density of 100 mA cm^{-2} in the electrolyte with HMF (1.330 V *vs.* RHE) is significantly lower than that for the OER at the same current density (1.630 V), indicating that the barrier for active species catalyzing HMFOR on $NiCo_2O_4$-mV is lower than that for the OER. Excitingly, $NiCo_2O_4$-mV only requires an input energy of 1.636 V to rapidly drive HMFOR at an industrial-level current density of 1 A cm^{-2} and to reach even an extreme current density of 1.329 A cm^{-2}, an input voltage of only 1.7 V is needed, demonstrating the outstanding commercial potential of $NiCo_2O_4$-mV. The HMFOR performances of different catalysts are shown in Fig. 3b and c, where $NiCo_2O_4$-mV significantly outperforms the reference samples $NiCo_2O_4$, NiCo LDH, and $Ni(OH)_2$ at current densities of 20, 50, 100, and 200 mA cm^{-2}, further confirming the high HMFOR activity of the mixed-cationic-defect $NiCo_2O_4$-mV. In addition, a series of $NiCo_2O_4$-mV samples synthesized at different temperatures was also prepared. As shown in Fig. S7c and d, the optimal HMFOR activity was shown by $NiCo_2O_4$-mV synthesized at 140 °C. The HMFOR activity of the optimal sample at 1.4 V significantly exceeded the performances of materials obtained at other temperatures, including 120 °C (95.23 mA cm^{-2}), 130 °C (124.77 mA cm^{-2}), and 150 °C (74.73 mA cm^{-2}). This enhanced activity emphasizes the catalyst temperature-induced surface ion dissolution under alkaline conditions, which promotes the oxidation of HMF, ultimately achieving the top of a volcano plot of HMFOR performance. Furthermore, the HMFOR performance of $NiCo_2O_4$-mV was compared with recently published works (Fig. 3d and Table S1). In a stark demonstration, $NiCo_2O_4$-mV exhibits superior performance compared to most HMFOR electrocatalysts.

Additionally, the double-layer capacitance (C_{dl}) was determined in the non-faradaic region by cyclic voltammetry (Fig. S8) to access the electrochemical active surface area (ECSA) values of different samples. As shown in Fig. 3e, the C_{dl} value of $NiCo_2O_4$-mV is 153 mF cm^{-2}, significantly higher than those of $NiCo_2O_4$ (81.2 mF cm^{-2}), NiCo LDH (5.0 mF cm^{-2}), and $Ni(OH)_2$ (4.37 mF cm^{-2}). The C_{dl} results indicate that compared with cationic-defect-free $NiCo_2O_4$ and hydroxide catalysts, $NiCo_2O_4$-mV has a larger ECSA and more exposed active sites, enabling superior electrochemical performance. Furthermore, optimal fitting of the interfacial charge transfer resistance (R_{ct}) revealed that compared with other reference samples, $NiCo_2O_4$-mV exhibited the lowest R_{ct} values at various potentials in electrolyte containing 50 mM HMF (Fig. S9). Specifically, as illustrated in Fig. S9, $NiCo_2O_4$-mV exhibits significantly lower R_{ct} values over the entire potential range, indicating that the adsorption of HMF molecules on the $NiCo_2O_4$-mV electrode interface is enhanced, thereby achieving rapid mass-transfer kinetics within the electric double-layer (EDL) structure. The open-circuit potential (OCP) was employed to evaluate the differentiation of organic adsorbates within the inner Helmholtz layer of the material. Upon the injection of 50 mM HMF into 1 M KOH solution, a rapid decline in the OCP was observed for both $NiCo_2O_4$-mV and $NiCo_2O_4$ (Fig. 3f), indicating that these catalysts possess rapid adsorption kinetics for HMF. In striking contrast, the OCP change for $NiCo_2O_4$-mV (0.461 V) was more pronounced than that for $NiCo_2O_4$ (0.417 V), supporting the idea that $NiCo_2O_4$-mV adsorbs a greater amount of HMF within the inner Helmholtz layer. Additionally, the catalytic selectivity of the obtained catalysts was verified using various substrates containing aldehyde and alcohol functional groups. As the LSV profiles in Fig. 3g show, $NiCo_2O_4$-mV exhibited superior electrooxidation activity towards 2-furaldehyde and furfuryl alcohol compared to $NiCo_2O_4$. At 1.4 V, the current densities for the electrooxidation of 2-furaldehyde and furfuryl alcohol by $NiCo_2O_4$-mV were 73 mA cm^{-2} and 103 mA cm^{-2}, respectively, which are higher than those of $NiCo_2O_4$ (50 mA cm^{-2} and 57 mA cm^{-2}, respectively). These results demonstrate that $NiCo_2O_4$-mV, with its mixed-ionic defects, possesses enhanced electrooxidation activity towards furfural and furfuryl alcohol.

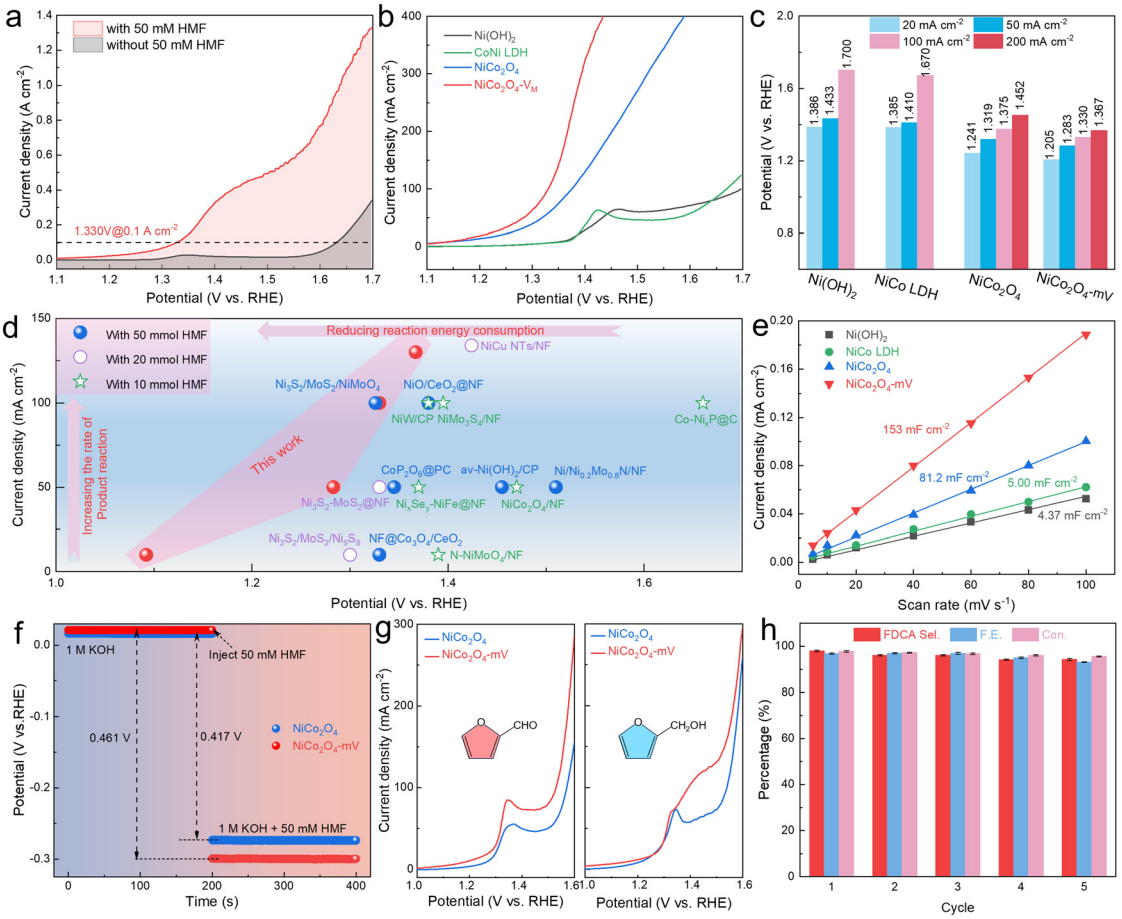

Fig. 3 (a) LSV profiles of $NiCo_2O_4$-mV in 1 M KOH with/without 50 mM HMF, (b) LSV profiles of different electrocatalysts in 1 M KOH with 50 mM HMF, and (c) the corresponding potential values at current densities of 20, 50, 100, and 200 mA cm^{-2}; (d) a comparison of the performance of $NiCo_2O_4$-mV with other advanced HMFOR electrocatalysts (the corresponding performance details can be seen in Table S1); (e) capacitive current densities for HMFOR at various scan rates for different electrocatalysts; (f) the OCP results for $NiCo_2O_4$-mV and $NiCo_2O_4$ in 1 M KOH solution before and after the injection of 50 mM HMF; (g) LSV curves for electrooxidation with $NiCo_2O_4$-mV and $NiCo_2O_4$ in 1 M KOH including 10 mM 2-furaldehyde or furfuryl alcohol; and (h) the HMF conversion, FDCA selectivity, and F.E. for five sequential electrolysis cycles of HMFOR using $NiCo_2O_4$-mV at 1.4 V.

The electro-oxidation of HMF was conducted in an H-type electrolysis cell to analyze the oxidation products. Typically, the oxidation of HMF to FDCA involves two potential pathways due to the coexistence of hydroxyl and aldehyde groups, as shown in Fig. S11. In pathway 1,[2,38] the aldehyde group is preferentially oxidized to a carboxyl group, leading to the formation of HMFCA. In pathway 2,[39] the hydroxyl group is oxidized to an aldehyde group, resulting in the formation of DFF. Fig. S12a and S12b shows that as the reaction time progresses, the peak intensity of HMF decreases (by up to 15C), while the peak intensity of FDCA increases. Meanwhile, the intermediate product HMFCA is detected, with its concentration first rising (not exceeding 1 mM) and then decreasing to approach ~0. Additionally, a small amount of FFCA intermediate is detected, while DFF shows a negligible signal, indicating that the HMFOR process derived from $NiCo_2O_4$-mV follows pathway 1 (HMF → HMFCA → FFCA → FDCA). Notably, $NiCo_2O_4$-mV exhibits impressive HMFOR performance, with a high HMF conversion rate of 96.7%, an FDCA yield of 96.6%, selectivity of 96.7%, and faradaic efficiency of 95.7%, surpassing most reported electrocatalysts (Table S2). To investigate the catalyst's cycling durability, five consecutive cycles were performed at 1.4 V to assess the durability of $NiCo_2O_4$-mV. As shown in Fig. 3h, the FDCA selectivity, faradaic efficiency, and HMF conversion rate all remain above 93% after five cycles, demonstrating the robust stability of $NiCo_2O_4$-mV.

3.3. Identification of the catalytic mechanism of the $NiCo_2O_4$-mV precatalyst

To explore the mechanism of the transformation of HMF molecules on the $NiCo_2O_4$-mV electrode surface, *in situ* attenuated total reflection surface-enhanced infrared absorption spectroscopy (ATR-SEIRAS) analysis was conducted during the HMFOR process. As shown in Fig. 4a, the downward peaks at 1017, 1121, 1525, and 1650 cm^{-1} represent the consumption of HMF. Notably, the upward peaks at 1356, 1389, and 1582 cm^{-1} represent the formation of HMFCA, while the upward peaks at 1256 and 1421 cm^{-1} are attributed to FFCA.[10] Moreover, the band at 1356 cm^{-1} can be attributed to symmetric stretching vibrations of carboxylic acid in FDCA and

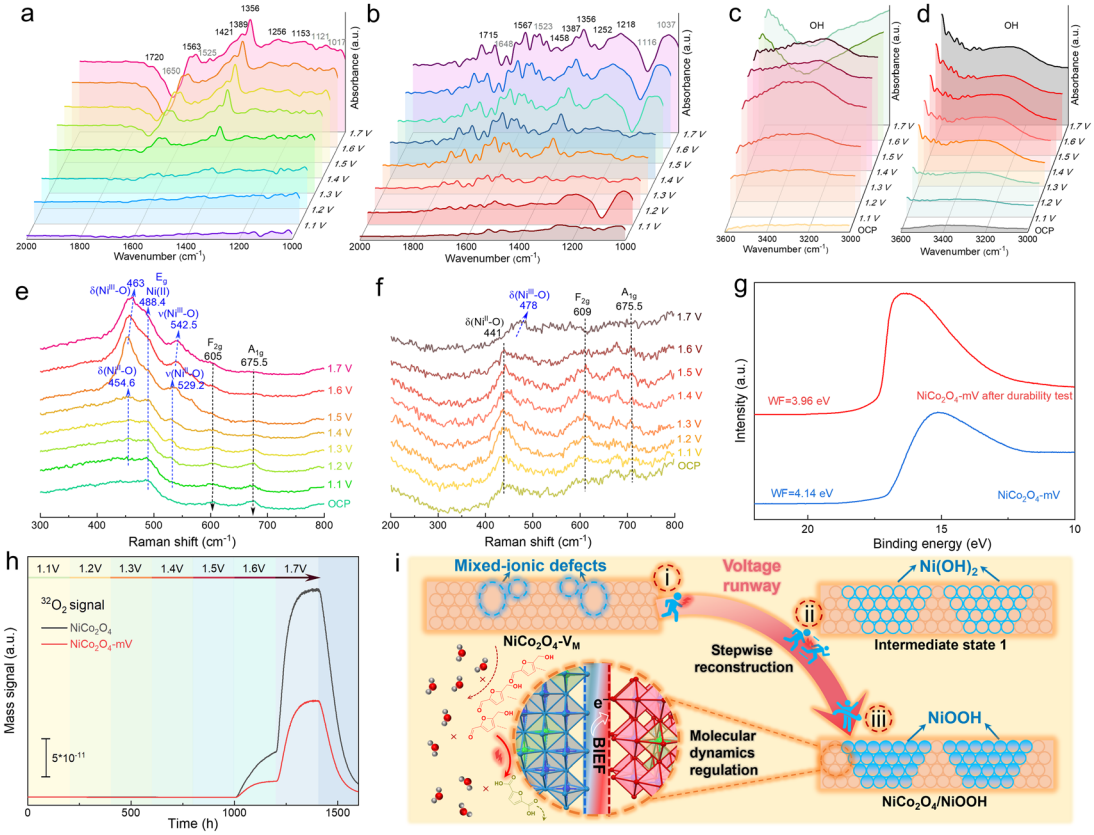

Fig. 4 *In situ* ATR-SEIRAS detection of (a) $NiCo_2O_4$-mV and (b) pristine $NiCo_2O_4$ for HMFOR in 1 M KOH electrolyte with 50 mM HMF at the wavenumber range of 1000–2000 cm^{-1}, and the corresponding wavenumber range of 3000–3600 cm^{-1} for (c) $NiCo_2O_4$-mV and (d) pristine $NiCo_2O_4$. *In situ* Raman analysis of (e) $NiCo_2O_4$-mV and (f) pristine $NiCo_2O_4$ for HMFOR in 1 M KOH electrolyte with 50 mM HMF, and (g) UPS spectra of $NiCo_2O_4$-mV and $NiCo_2O_4$-mV after durability test. (h) The *operando* DE-MS detection of $NiCo_2O_4$-mV and pristine $NiCo_2O_4$ samples during HMFOR process. (i) Schematic illustration potential catalytic mechanism of the structure evolution of the $NiCo_2O_4$-mV pre-catalyst and the regulation interfacial adsorbed water induced by m-Ds.

FFCA.[37] The band at 1389 cm^{-1} can be attributed to the formation of FDCA.[37] Moreover, the peak intensities at 1017 and 1121 cm^{-1} gradually decrease, while the peak intensities at 1356, 1389, and 1582 cm^{-1} significantly increase, indicating the consumption of HMF and the formation of HMFCA and FDCA. The above ATR-SEIRAS analysis results confirm again that the transformation mechanism of HMF on the $NiCo_2O_4$-mV surface proceeds *via* the HMFCA path, consistent with the corresponding HPLC and Bode plots results (Fig. S13) for $NiCo_2O_4$-mV. Although the transformation of HMF on $NiCo_2O_4$ also follows the HMFCA mechanism (Fig. 4b), the corresponding characteristic peak intensities are significantly reduced compared to $NiCo_2O_4$-mV, indicating that $NiCo_2O_4$-mV, with its mixed-defect structure, is more efficient in electrocatalytic HMFOR than $NiCo_2O_4$.

To further elucidate the role of m-Ds in the catalyst and HMFOR, electrochemical *in situ* Raman analysis was conducted during the electrocatalyst process with and without HMF. As shown in Fig. 4e, when using 1 M KOH solution with 50 mM HMF, at the open-circuit potential (OCP), $NiCo_2O_4$-mV exhibited distinct vibrational signals attributed to the E_g, F_{2g}, and A_{1g} modes of $NiCo_2O_4$ at 488.4, 605, and 675.5 cm^{-1}, respectively, supporting the overall crystalline integrity of $NiCo_2O_4$-mV.[40] More importantly, as the applied potential increased to 1.2 V, two clear peak appeared at 454.6 and 529.2 cm^{-1}, which were correspondingly attributed to the vibration signals of Ni^{II}–O in $Ni(OH)_2$ crystals and of Ni^{II}–O from A_{1g} stretching vibration signals of defective or disordered $NiCo(OH)_2$ that evolved on the $NiCo_2O_4$ surface under alkaline conditions, respectively.[26] Concurrently, the disordered or defective vibrations at 529.2 cm^{-1} became more pronounced than the signal at 454.6 cm^{-1}, supporting the evolution of more $NiCo_2O_4$ on the $NiCo_2O_4$-mV surface into disordered or defective $NiCo(OH)_2$ at low potentials, which would lead to the exposure of more coordinatively unsaturated active sites, supporting the high activity of HMFOR at low potentials. Importantly, as the potential continued to rise to a high potential of 1.7 V, the vibrational signal of $NiCo_2O_4$-mV at 454.6 cm^{-1} shifted positively to 463 cm^{-1} with a rapid increase in signal intensity, which was attributed to the E_g stretching vibration signal of Ni^{III}–O in surface-evolved NiCoOOH.[24,41] Additionally, the weak characteristic peak at 529.2 cm^{-1} further shifted positively to 542.5 cm^{-1}, supporting the A_{1g} stretching vibration mode of Ni^{III}–O in surface-reconstructed

NiCoOOH.[24,26] Moreover, the F_{2g} and A_{1g} vibrational signals of $NiCo_2O_4$-mV showed a decreasing trend with an increase in potential, further supporting potential-dependent surface reconstruction on the $NiCo_2O_4$-mV surface. In stark contrast, pristine $NiCo_2O_4$ exhibited negligible surface structural changes with an increase in potential (Fig. 4f). Such results clearly demonstrate that the presence of m-Ds in $NiCo_2O_4$-mV facilitates the partial evolution of the $NiCo_2O_4$ surface into defect-rich $NiCo(OH)_2$ at low potentials, further generating NiCoOOH in a high oxidation state as the potential continues to rise to higher potentials; that is, the partial evolution trend is $NiCo_2O_4 \rightarrow NiCo(OH)_2 \rightarrow$ NiCoOOH. HR-TEM and XPS analysis of $NiCo_2O_4$-mV after long-term stability testing (Fig. S14 and S15) clearly showed the closely contacted interface between hydroxide/hydroxide oxide and $NiCo_2O_4$. These findings indicate that compared with pristine $NiCo_2O_4$, the surface of $NiCo_2O_4$-mV with m-Ds is more prone to partial evolution into $NiCo(OH)_2$ and/or NiCoOOH under alkaline conditions, forming an $NiCo_2O_4$/NiCoOOH heterojunction with the bulk $NiCo_2O_4$ surface.

It is well-known that hydroxides/hydroxide oxides generally exhibit excellent activity in alkaline biomass electro-oxidation systems. To demonstrate the contribution of *in situ* reconstructed hydroxide/hydroxide oxide toward HMFOR performance, $NiCo_2O_4$-mV grown on carbon paper was fully transformed into hydroxide/hydroxide oxide *via* long-term activation at a high voltage (1.8 V for 12 h) or high current density (600 mA cm^{-2} for 12 h). The XRD patterns of the activated samples showed the characteristic peaks of nickel/cobalt-based hydroxide/hydroxide oxide (Fig. S16a and S16b), indicating the complete transformation of $NiCo_2O_4$-mV into nickel/cobalt-based hydroxide/hydroxide oxide. Importantly, electrochemical performance results (Fig. S16c and S16d) showed that this nickel/cobalt-based hydroxide/hydroxide oxide exhibited inferior HMFOR performance compared to $NiCo_2O_4$-mV, suggested that even at high potentials, the HMFOR performance is mainly derived from $NiCo_2O_4$.

Relevantly, previous reports have indicated that the formation of hydroxide heterojunctions leads to the creation of a BIEF at the heterojunction interface, thereby affecting the adsorption and desorption of interfacial water and HMF molecules at the electrode–electrolyte interface (*i.e.*, the EDL), as well as the mass-transfer kinetics of HMF molecules.[42] The influence of mixed-ionic defects on the adsorption kinetics of surface-adsorbed water molecules at the electrode–solution interface was further investigated by *in situ* ATR-SEIRAS technology. As shown in Fig. 4d, for a pristine $NiCo_2O_4$ electrode, the intensity of the O–H stretching vibration band of interfacial water (located at ~3400 cm^{-1}) increases with potential, indicating an increase in the interfacial H_2O concentration at the $NiCo_2O_4$ surface. When $NiCo_2O_4$ is combined with m-Ds (Fig. 4c), the intensity of the O–H stretching vibration signal first increases and then significantly decreases with a gradual rise in potential, suggesting that the concentration of interfacial H_2O decreases as the potential becomes more positive, accompanied by the weakening of hydrogen bonds in the EDL, thereby promoting the migration of HMF molecules from bulk solution to the electrode–solution interface, leading to the enhancement of HMFOR kinetics, which is consistent with the EIS results (Fig. S9 and S10). In contrast, the $NiCo_2O_4$ sample shows a continuously increasing interfacial water concentration, which might hinder the mass transfer of HMF molecules at the electrode–electrolyte interface, thereby suppressing the activity and selectivity of HMFOR. Importantly, *in situ* Raman spectroscopy analysis (Fig. S17) also reveals that strong hydrogen-bonded water in $NiCo_2O_4$-mV exhibits a systematic decrease, whereas weak hydrogen-bonded water shows an elusive change.[31] This observation indicates that $NiCo_2O_4$-mV induces a significant reduction in interfacial water with strong hydrogen bonds, which is consistent with the findings from *in situ* ATR-SEIRAS analysis.

To explore the existence of the BIEF, UPS was used to obtain the work function (φ) of the two components forming the heterojunction, thereby assessing the directional electron transfer behavior at the heterojunction interface. As shown in Fig. 4g, the calculated φ values for NiCoO(OH) (formed from $NiCo_2O_4$ after durability testing) and $NiCo_2O_4$-mV are 3.96 eV and 4.14 eV, respectively, showing a relatively large $\Delta\varphi$ of 0.18 eV at the NiCoO(OH)–$NiCo_2O_4$ interface, indicating that electrons flow from NiCoO(OH) with the lower φ value to $NiCo_2O_4$-mV with the higher φ value, thereby inducing the formation of a BIEF at the NiCoO(OH)–$NiCo_2O_4$ interface. The aforementioned results demonstrate the existence of the BIEF at the NC/NiCoO(OH) heterojunction with directional charge transfer (electrons from NiCoO(OH) to $NiCo_2O_4$-mV), leading to the uneven distribution of the valence states of Ni/Co sites at the interface, which might cause an imbalance in the force intensity of interfacial water at the EDL, thereby disrupting the directional arrangement and adsorption concentration of interfacial water. Furthermore, the rigid hydrogen-bond network formed by interfacial H_2O and OH^- at the electrode–electrolyte interface greatly restricts the diffusion distribution of HMF.[33] In contrast, the looser hydrogen-bond environment on the heterojunction surface allows for a higher distribution intensity of HMF at the interface, thereby enhancing the activity and selectivity of HMFOR. The aforementioned speculation was further verified by *operando* DE-MS. As shown in Fig. 4h, in alkaline medium containing HMF, no $^{32}O_2$ signal was detected for $NiCo_2O_4$ and $NiCo_2O_4$-mV in the medium-low potential range (1.2–1.5 V), indicating that the HMFOR process selectively occurs in the aforementioned potential interval. When the applied potential rises to the high potential range (1.6–1.7 V), a distinct $^{32}O_2$ signal can be detected and this rapidly increases with an increase in the applied potential. At the same time, the $^{32}O_2$ signal continuously accumulates with the extension of the reaction time. Those results indicate that although both $NiCo_2O_4$ and $NiCo_2O_4$-mV exhibit OER activity at high potentials, and the activity increases with an increase in the applied potential, it is evident that the $^{32}O_2$ signal of $NiCo_2O_4$-mV is significantly lower than that of the $NiCo_2O_4$ catalyst, indicating that the internal electric field in the $NiCo_2O_4$/NiCoO(OH) heterojunction significantly inhibits the

adsorption of interfacial water, thereby enhancing the activity and selectivity of HMFOR.

Therefore, we propose a potential mechanism for the electrocatalytic oxidation of HMF by $NiCo_2O_4$-mV with mixed-ionic defects. As shown in Fig. 4i, when the voltage increases from the OCP to medium-low potentials, under alkaline conditions, the surface/interface of $NiCo_2O_4$-mV with mixed-ionic defect species is prone to partial evolution into hydroxides. This is perhaps because the presence of defect sites promotes the evolution of lattice oxygen near the defect sites into lattice hydroxyl groups, accompanied by the generation of more defect species. Due to the high reactivity and structural instability around the defect sites, this ultimately leads to the improvement of HMFOR performance at low potentials. Furthermore, as the voltage rises to high voltages, driven by the potential energy, a large amount of disordered and defective $NiCo_2O_4$ and/or $Ni(OH)_2$ will further evolve into NiOOH species with high HMFOR activity. More importantly, when $NiCo_2O_4$ with a different work function comes into close contact with NiOOH, an $NiCo_2O_4$/NiCoOOH heterojunction is formed which induces the formation of a large BIEF at the interface, due to the spontaneous flow of electrons causing charge redistribution. Furthermore, the charge density around the active centers is disrupted by the BIEF, further weakening the strength of hydrogen bonds between the adsorbed water or interfacial water and the adsorbed species on the heterojunction surface/interface, prompting a decrease in the concentration of adsorbed water or interfacial water on the surface of $NiCo_2O_4$-mV, while enhancing the selective adsorption and efficient mass transfer of HMF molecules on the surface of $NiCo_2O_4$-mV, ultimately improving the activity and selectivity of HMFOR.

3.4. Electrochemical performance of practical devices

To investigate the operational efficiency of $NiCo_2O_4$-mV in practical devices, an anion exchange membrane electrolyzer was assembled using $NiCo_2O_4$-mV (1 cm × 1 cm) and nickel foam as the anode and cathode, respectively, for the continuous valorization of HMF at a concentration of 100 mM (Fig. 5a and Fig. S19). As shown in Fig. 5b, the current density of the $NiCo_2O_4$-mV catalyst for the HMFOR‖HER pair is significantly higher than that of the OER‖HER pair, achieving a high current of up to ~550 mA cm^{-2} at a voltage of 2.2 V. Moreover, with this electrolyzer, HMF can be stably converted at 1.65 V when the electrolyte flow rate is approximately 15 mL min^{-1}, with a unidirectional conversion rate exceeding 84.8% (Fig. 5c). To enhance the cyclic conversion efficiency of HMF, an electrolyzer was used to simulate the up-cycling process of HMFOR in series configuration. $NiCo_2O_4$-mV can operate continuously and stably for ~180 hours. After nine cycles, the conversion rate of HMF approaches 93%. Therefore, the aforementioned work not only reveals the high activity and excellent selectivity of $NiCo_2O_4$-mV in the continuous up-cycling of HMF but also, importantly, it indicates the great potential of $NiCo_2O_4$-mV in the industrial upgrading of HMF to FDCA.

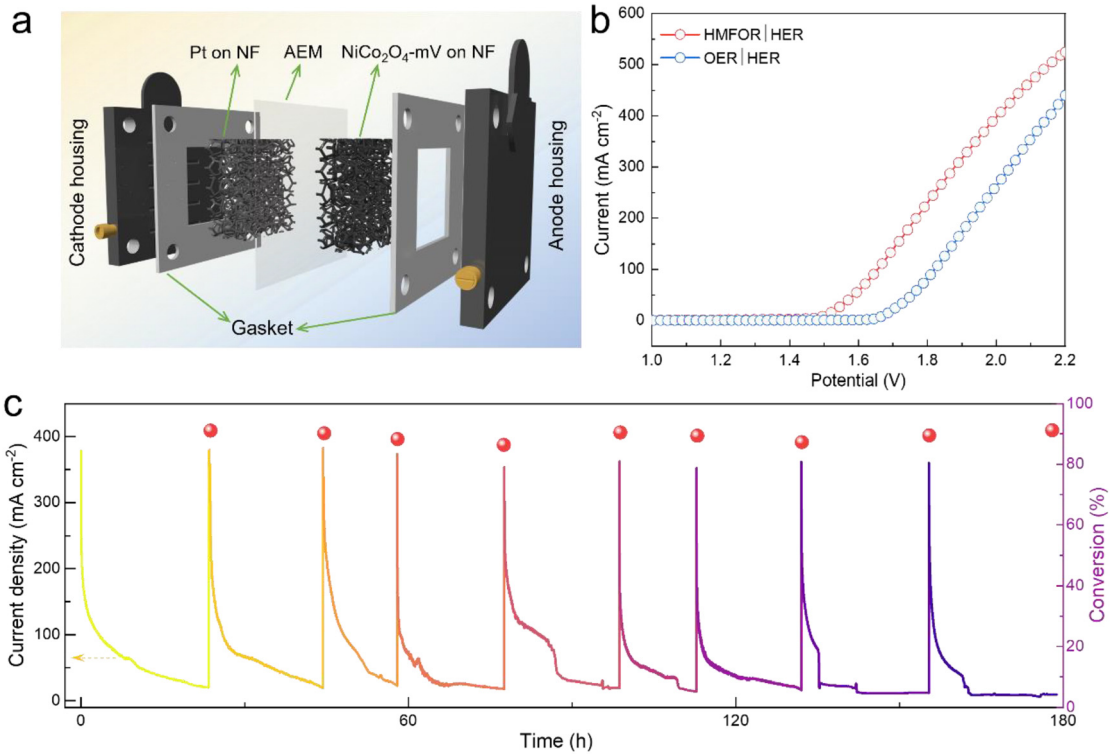

Fig. 5 (a) A schematic diagram of the anion–exchange membrane electrolyzer used in the coupled HMFOR/HER system; (b) LSV curves for the AEM electrolyzer in 1 M KOH with and without 100 mM HMF; and (c) plots of current density and the conversion of HMF *vs.* time during continuous operation for 180 h.

4. Conclusions

In summary, we report the incorporation of mixed-ionic defects into $NiCo_2O_4$-mV, which is attributed to hydrothermal processes involving $NiCo_2O_4$ in alkaline solution. The resulting defective $NiCo_2O_4$-mV is characterized by more oxidative $Ni^{(2+\delta)+}$ and $Co^{(2+\delta)+}$ ($0 < \delta < 1$) species and longer Ni–O bond lengths and M–M (M = Ni or Co) distances compared to pristine $NiCo_2O_4$. *In situ* Raman spectroscopy indicates that upon increasing the applied voltage, the surface of $NiCo_2O_4$-mV undergoes partial evolution from $NiCo_2O_4$ → $Ni(OH)_2$ → NiOOH (with high HMFOR activity). More importantly, *in situ* ATR-SEIRAS and DE-MS measurements confirm the presence of a significant spatially oscillating BIEF at the interface induced by the mixed-ionic-defect $NiCo_2O_4$/NiCoO(OH) heterojunction, which further affects the heterojunction's suppression of surface-adsorbed water molecules and the rapid adsorption and mass transfer of HMF, accounting for the high activity, industrial-level current density, and selectivity of the $NiCo_2O_4$-mV precatalyst in the HMFOR process. This work provides deep insights into the evolution behavior of defect engineering and its crucial role in enhancing the activity and selectivity of precatalysts for the electrochemical upgrading of biomass.

Author contributions

The manuscript was written through contributions from all authors. All authors have given approval to the final version of the manuscript.

Conflicts of interest

The authors declare that they have no known competing financial interests or personal relationships that could have appeared to influence the work reported in this paper.

Data availability

The data supporting this article have been included as part of the SI.

Supplementary information: additional SEM, TEM, XRD, XPS, WT-EXAFS and electrochemical data. See DOI: **https://doi.org/10.1039/d5gc03049h**.

Acknowledgements

This work was supported by the National Natural Science Foundation of China (No. 52301271), the Natural Science Foundation of Hunan Province (No. 2024JJ6097), China Postdoctoral Science Foundation (No. 2024000053), Postdoctoral Science Foundation of Anhui Province (No. 2024000379), and the Academic College Student Innovation and Entrepreneurship Training Program (S202210546010). We thank Prof. Dr Huajie Yin for his support with *in situ* Raman and DE-MS measurements and Prof. Dr Haimin Zhang for his support with *in situ* ATR-SEIRAS measurements, respectively, at the Institute of Solid State Physics.

References

1 H. G. Cha and K.-S. Choi, Combined biomass valorization and hydrogen production in a photoelectrochemical cell, *Nat. Chem.*, 2015, **7**, 328–333, DOI: **10.1038/nchem.2194**.
2 X. Wu, Y. Wang and Z.-S. Wu, Design principle of electrocatalysts for the electrooxidation of organics, *Chem*, 2022, **8**, 2594–2629, DOI: **10.1016/j.chempr.2022.07.010**.
3 H. Y. Wang, M. L. Sun, J. T. Ren and Z. Y. Yuan, Circumventing challenges: design of anodic electrocatalysts for hybrid water electrolysis systems, *Adv. Energy Mater.*, 2022, **13**, 2203568, DOI: **10.1002/aenm.202203568**.
4 Y. Lu, T. Liu, Y.-C. Huang, L. Zhou, Y. Li, W. Chen, L. Yang, B. Zhou, Y. Wu, Z. Kong, Z. Huang, Y. Li, C.-L. Dong, S. Wang and Y. Zou, Integrated catalytic sites for highly efficient electrochemical oxidation of the aldehyde and hydroxyl groups in 5-hydroxymethylfurfural, *ACS Catal.*, 2022, **12**, 4242–4251, DOI: **10.1021/acscatal.2c00174**.
5 W. Chen, C. Xie, Y. Wang, Y. Zou, C.-L. Dong, Y.-C. Huang, Z. Xiao, Z. Du, S. Wei, C. Chen, B. Zhou, J. Ma and S. Wang, Activity origins and design principles of nickel-based catalysts for nucleophile electrooxidation, *Chem*, 2020, **6**, 2974–2993, DOI: **10.1016/j.chempr.2020.07.022**.
6 X. Liu, X. Wang, C. Mao, J. Qiu, R. Wang, Y. Liu, Y. Chen and D. Wang, Ligand–hybridization activates lattice–hydroxyl–groups of $NiCo(OH)_x$ nanowires for efficient electrosynthesis, *Angew. Chem., Int. Ed.*, 2024, **63**, e202408109, DOI: **10.1002/anie.202408109**.
7 W.-J. Liu, L. Dang, Z. Xu, H.-Q. Yu, S. Jin and G. W. Huber, Electrochemical oxidation of 5-hydroxymethylfurfural with NiFe layered double hydroxide (LDH) nanosheet catalysts, *ACS Catal.*, 2018, **8**, 5533–5541, DOI: **10.1021/acscatal.8b01017**.
8 J. Zhang, Y. Shen, Z. Wu, X. Zhang, J. Kang, Y. Wu, S. Zhang, S. Chen, G. Wang, H. Zhang, H. Yin and H. Zhao, Efficient alkaline-free electrooxidation of 5-hydroxymethylfurfural to 2,5-furandicarboxylic acid using electrochemically-charged $Ni_xCo_{1-x}(OH)_2$ as a redox mediator, *Angew. Chem., Int. Ed.*, 2025, **64**, e202423109, DOI: **10.1002/anie.202423109**.
9 S. Wang, H. Feng, T. Liu, Y. Deng, M. Zhang, S. Zhao, J. Han and X. Zhang, Theoretical exploration of the origin of alkaline dependence in the oxidation of 5-hydroxymethylfurfural catalyzed by NiO_2H_x, *ACS Catal.*, 2024, **14**, 9860–9869, DOI: **10.1021/acscatal.4c00940**.
10 Z. Zhou, Y.-N. Xie, L. Sun, Z. Wang, W. Wang, L. Jiang, X. Tao, L. Li, X.-H. Li and G. Zhao, Strain-induced in situ formation of NiOOH species on Co-Co bond for selective electrooxidation of 5-hydroxymethylfurfural and efficient

hydrogen production, *Appl. Catal., B*, 2022, **305**, 121072, DOI: 10.1016/j.apcatb.2022.121072.

11 T. Wu, Z. Xu, X. Wang, M. Luo, Y. Xia, X. Zhang, J. Li, J. Liu, J. Wang, H.-L. Wang and F. Huang, Surface-confined self-reconstruction to sulfate-terminated ultrathin layers on $NiMo_3S_4$ toward biomass molecule electro-oxidation, *Appl. Catal., B*, 2023, **323**, 122126, DOI: 10.1016/j.apcatb.2022.122126.

12 B. You, X. Liu, N. Jiang and Y. Sun, A general strategy for decoupled hydrogen production from water splitting by integrating oxidative biomass valorization, *J. Am. Chem. Soc.*, 2016, **138**, 13639–13646, DOI: 10.1021/jacs.6b07127.

13 H. Wang, Y. Zhou and S. Tao, CoP-CoOOH heterojunction with modulating interfacial electronic structure: a robust biomass-upgrading electrocatalyst, *Appl. Catal., B*, 2022, **315**, 121588, DOI: 10.1016/j.apcatb.2022.121588.

14 R. Luo, Y. Li, L. Xing, N. Wang, R. Zhong, Z. Qian, C. Du, G. Yin, Y. Wang and L. Du, A dynamic $Ni(OH)_2$-NiOOH/NiFeP heterojunction enabling high-performance e-upgrading of hydroxymethylfurfural, *Appl. Catal., B*, 2022, **311**, 121357, DOI: 10.1016/j.apcatb.2022.121357.

15 Y. Li, K. Alorku, C. Shen, L. Yan, Q. Li, X. Tian, W. Li, Y. Xu, C. Wang, C. Li, L. Ma, H. Duan, Q. Liu and J. Jiang, *In situ* redispersion of Ni@C catalyst boosts 5-hydroxymethylfurfural electrooxidation by increasing Ni^{4+} sites, *Appl. Catal., B*, 2024, **357**, 124250, DOI: 10.1016/j.apcatb.2024.124250.

16 W. Guo, X. Cao, D. Tan, B. Wulan, J. Ma and J. Zhang, Thermal–driven dispersion of bismuth nanoparticles among carbon matrix for efficient carbon dioxide reduction, *Angew. Chem., Int. Ed.*, 2024, **63**, e202401333, DOI: 10.1002/anie.202401333.

17 S. Barwe, J. Weidner, S. Cychy, D. M. Morales, S. Dieckhöfer, D. Hiltrop, J. Masa, M. Muhler and W. Schuhmann, Electrocatalytic oxidation of 5-(hydroxymethyl)furfural using high–surface–area nickel boride, *Angew. Chem., Int. Ed.*, 2018, **57**, 11460–11464, DOI: 10.1002/anie.201806298.

18 N. Huang, B. Chu, D. Chen, B. Shao, Y. Zheng, L. Li, X. Xiao and Q. Xu, Rational design of a quasi-metal–organic framework by ligand engineering for efficient biomass upgrading, *J. Am. Chem. Soc.*, 2025, **147**, 8832–8840, DOI: 10.1021/jacs.5c00294.

19 S. Yang, Y. Guo, P. Zhao, H. Jiang, H. Shen, Z. Chen, L. Jiang, X. Xue, Q. Zhang and H. Zhang, Unraveling the electrooxidation mechanism of 5-(hydroxymethyl)furfural at a molecular level via nickel-based two-dimensional metal–organic frameworks catalysts, *ACS Catal.*, 2024, **14**, 449–462, DOI: 10.1021/acscatal.3c04977.

20 J. Kang, X. Qiu, Q. Hu, J. Zhong, X. Gao, R. Huang, C. Wan, L.-M. Liu, X. Duan and L. Guo, Valence oscillation and dynamic active sites in monolayer NiCo hydroxides for water oxidation, *Nat. Catal.*, 2021, **4**, 1050–1058, DOI: 10.1038/s41929-021-00715-w.

21 S. Yang, X. Xiang, Z. He, W. Zhong, C. Jia, Z. Gong, N. Zhang, S. Zhao and Y. Chen, Anionic defects engineering of $NiCo_2O_4$ for 5-hydroxymethylfurfural electrooxidation, *Chem. Eng. J.*, 2023, **457**, 141344, DOI: 10.1016/j.cej.2023.141344.

22 X. Deng, G. Y. Xu, Y. J. Zhang, L. Wang, J. Zhang, J. F. Li, X. Z. Fu and J. L. Luo, Understanding the roles of electrogenerated Co^{3+} and Co^{4+} in selectivity-tuned 5-hydroxymethylfurfural oxidation, *Angew. Chem., Int. Ed.*, 2021, **60**, 20535–20542, DOI: 10.1002/anie.202108955.

23 Y. Lu, C. L. Dong, Y. C. Huang, Y. Zou, Z. Liu, Y. Liu, Y. Li, N. He, J. Shi and S. Wang, Identifying the geometric site dependence of spinel oxides for the electrooxidation of 5-hydroxymethylfurfural, *Angew. Chem., Int. Ed.*, 2020, **59**, 19215–19221, DOI: 10.1002/ange.202007767.

24 Y. Zhang, J. Liu, Y. Xu, C. Xie, S. Wang and X. Yao, Design and regulation of defective electrocatalysts, *Chem. Soc. Rev.*, 2024, **53**, 10620–10659, DOI: 10.1039/d4cs00217b.

25 Y.-J. Wu, J.-Z. Zheng, X. Zhou, T.-X. Tu, Y. Liu, P.-F. Zhang, L. Tan and S. Zhao, Cationic defect-enriched hydroxides as anodic catalysts for efficient seawater electrolysis, *Inorg. Chem. Front.*, 2023, **10**, 2444–2456, DOI: 10.1039/d3qi00026e.

26 Y. J. Wu, J. Yang, T. X. Tu, W. Q. Li, P. F. Zhang, Y. Zhou, J. F. Li, J. T. Li and S. G. Sun, Evolution of cationic vacancy defects: a motif for surface restructuration of OER precatalyst, *Angew. Chem., Int. Ed.*, 2021, **60**, 26829–26836, DOI: 10.1002/anie.202112447.

27 B. Liu, Y. Wang, H. Q. Peng, R. Yang, Z. Jiang, X. Zhou and C. S. Lee, H. Zhao, W. Zhang, Iron vacancies induced bifunctionality in ultrathin feroxyhyte nanosheets for overall water splitting, *Adv. Mater.*, 2018, **30**, 1803144, DOI: 10.1002/adma.201803144.

28 L. Gao, X. Cui, C. D. Sewell, J. Li and Z. Lin, Recent advances in activating surface reconstruction for the high-efficiency oxygen evolution reaction, *Chem. Soc. Rev.*, 2021, **50**, 8428–8469, DOI: 10.1039/d0cs00962h.

29 X. Zhao, M. Liu, Y. Wang, Y. Xiong, P. Yang, J. Qin, X. Xiong and Y. Lei, Designing a built-in electric field for efficient energy electrocatalysis, *ACS Nano*, 2022, **16**, 19959–19979, DOI: 10.1021/acsnano.2c09888.

30 C. Ni, K. Wang, L. Jin, Y. Liu, J. Chen, L. Yang, C. Ji, H. Xu, Z. Li and L. Tian, Built-in electric field guides oxygen evolution electrocatalyst reconstruction, *Chem. Commun.*, 2025, **61**, 658–668, DOI: 10.1039/D4CC04740K.

31 Z. Yang, L. Chen, Y. Yin, C. Wei, Z. Xue and T. Mu, Weakened hydrogen bond connectivity promotes interfacial mass transfer for industrial level scalable biomass electrooxidation, *Energy Environ. Sci.*, 2024, **17**, 8801–8809, DOI: 10.1039/d4ee03482a.

32 F. L. Crane, J. L. Glenn and D. E. Green, Studies on the electron transfer system IV. the electron transfer particle, *Biochim. Biophys. Acta*, 1956, **22**, 475–487, DOI: 10.1016/0006-3002(56)90058-0.

33 J. Zheng, X. Peng, Z. Xu, J. Gong and Z. Wang, Cationic defect engineering in spinel $NiCo_2O_4$ for enhanced electrocatalytic oxygen evolution, *ACS Catal.*, 2022, **12**, 10245–10254, DOI: 10.1021/acscatal.2c01825.

34 J. Ge, W. Zhang, J. Tu, T. Xia, S. Chen and G. Xie, Suppressed Jahn–Teller distortion in $MnCo_2O_4$@Ni_2P heterostructures to promote the overall water splitting, *Small*, 2020, **16**, 2001856, DOI: **10.1002/smll.202001856**.

35 Y. Zheng, H. Xie, J. Li, K. S. Hui, Z. Yu, H. Xu, D. A. Dinh, Z. Ye, C. Zha and K. N. Hui, Insights into the Jahn–Teller effect in layered oxide cathode materials for potassium–ion batteries, *Adv. Energy Mater.*, 2024, **14**, 2400461, DOI: **10.1002/aenm.202400461**.

36 X. Li, Z. Cheng and X. Wang, Understanding the mechanism of the oxygen evolution reaction with consideration of spin, *Electrochem. Energy Rev.*, 2020, **4**, 136–145, DOI: **10.1007/s41918-020-00084-1**.

37 P. Koley, S. C. Shit, T. Yoshida, H. Ariga-Miwa, T. Uruga, T. Hosseinnejad, S. Periasamy, S.-I. In, D. D. Mandaliya, R. D. Gudi, Y. Iwasawa and S. K. Bhargava, Elucidation of active sites and mechanistic pathways of a heteropolyacid/Cu-metal–organic framework catalyst for selective oxidation of 5-hydroxymethylfurfural via ex situ X-ray absorption spectroscopy and in situ attenuated total reflection-infrared studies, *ACS Catal.*, 2023, **13**, 6076–6092, DOI: **10.1021/acscatal.3c00872**.

38 C. Chen, M. Lv, H. Hu, L. Huai, B. Zhu, S. Fan, Q. Wang and J. Zhang, 5-Hydroxymethylfurfural and its downstream chemicals: a review of catalytic routes, *Adv. Mater.*, 2024, **36**, 2311464, DOI: **10.1002/adma.202311464**.

39 O. Simoska, Z. Rhodes, S. Weliwatte, J. R. Cabrera-Pardo, E. M. Gaffney, K. Lim and S. D. Minteer, Advances in electrochemical modification strategies of 5-hydroxymethylfurfural, *ChemSusChem*, 2021, **14**, 1674–1686, DOI: **10.1002/cssc.202100139**.

40 M. N. Iliev, P. Silwal, B. Loukya, R. Datta, D. H. Kim, N. D. Todorov, N. Pachauri and A. Gupta, Raman studies of cation distribution and thermal stability of epitaxial spinel $NiCo_2O_4$ films, *J. Appl. Phys.*, 2013, **114**, 033514, DOI: **10.1063/1.4815874**.

41 X. Jiang, X. Ma, Y. Liu, L. Zhao, Y. Zhang, B.-Q. Li and Q. Zhang, Cation vacancies creation propel pre-oxidation enhancing nickel hydroxide activity for highly efficient 5-hydroxymethylfurfural upgrading, *Appl. Catal., B*, 2024, **347**, 123785, DOI: **10.1016/j.apcatb.2024.123785**.

42 K. Ji, Y. Liu, Y. Wang, K. Kong, J. Li, X. Liu and H. Duan, Steering selectivity in electrocatalytic furfural reduction via electrode–electrolyte interface modification, *J. Am. Chem. Soc.*, 2024, **146**, 11876–11886, DOI: **10.1021/jacs.4c00818**.